

In the format provided by the authors and unedited.

Rapid expansion of Greenland's low-permeability ice slabs

M. MacFerrin^{1*}, H. Machguth^{2,3}, D. van As⁴, C. Charalampidis⁵, C. M. Stevens⁶, A. Heilig^{7,8,9}, B. Vandecrux^{4,10}, P. L. Langen¹¹, R. Mottram¹¹, X. Fettweis¹², M. R. van den Broeke¹³, W. T. Pfeffer¹⁴, M. S. Moussavi^{1,15} & W. Abdalati¹

¹Cooperative Institute for Research in Environmental Sciences, University of Colorado, Boulder, CO, USA. ²Department of Geosciences, University of Fribourg, Fribourg, Switzerland. ³Department of Geography, University of Zurich, Zurich, Switzerland. ⁴Geological Survey of Denmark and Greenland, Copenhagen, Denmark. ⁵Bavarian Academy of Sciences and Humanities, Munich, Germany. ⁶Department of Earth and Space Sciences, University of Washington, Seattle, WA, USA. ⁷WSL Institute for Snow and Avalanche Research SLF, Davos Dorf, Switzerland. ⁸Department of Earth and Environmental Sciences, Ludwig-Maximilians-University of Munich, Munich, Germany. ⁹Alfred Wegener Institute Helmholtz-Centre for Polar and Marine Research, Bremerhaven, Germany. ¹⁰Department of Civil Engineering, Technical University of Denmark, Kongens Lyngby, Denmark. ¹¹Danish Meteorological Institute, Copenhagen, Denmark. ¹²Department of Geography, University of Liège, Liège, Belgium. ¹³Institute for Marine and Atmospheric Research, Utrecht University, Utrecht, The Netherlands. ¹⁴Department of Civil Engineering, University of Colorado, Boulder, CO, USA. ¹⁵National Snow and Ice Data Center, University of Colorado, Boulder, CO, USA. *e-mail: michael.macferrin@colorado.edu

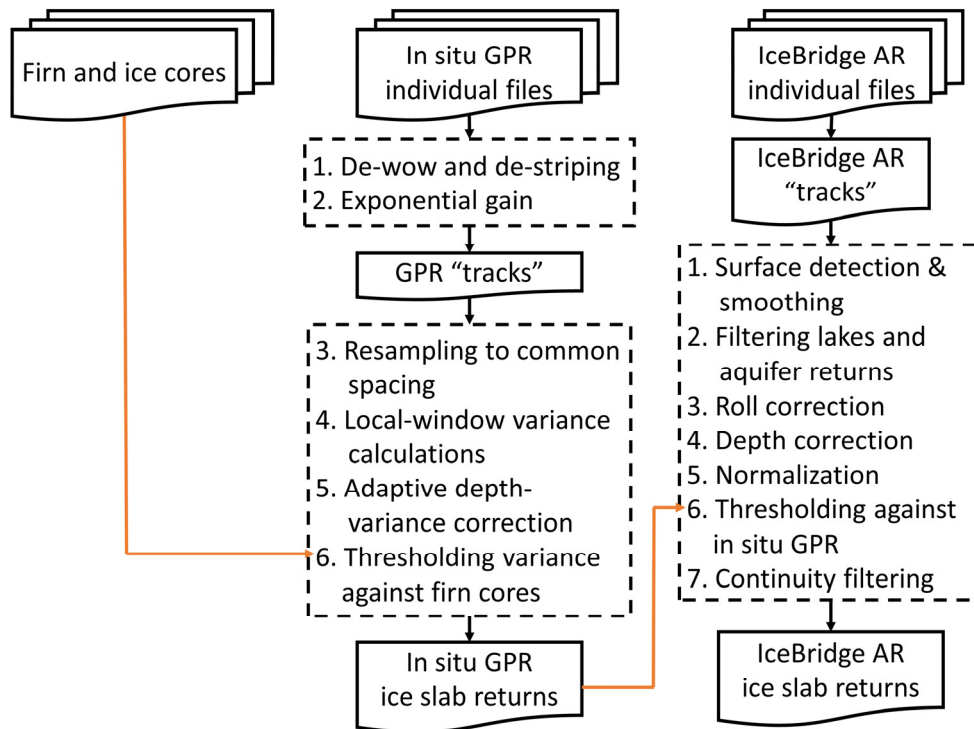
Rapid expansion of Greenland’s low-permeability ice slabs

MacFerrin, M., Machguth, H., van As, D., Charalampidis, C., Stevens, C., Heilig, A., Vandecrux, B, Langen, P., Mottram, R., Fettweis, X., Van den Broeke, M. R., Pfeffer, T., Moussavi, M., Abdalati, W.

Correspondence: Michael MacFerrin, Michael.MacFerrin@Colorado.edu

— Supplementary Information —

In this supplement, “GPR” refers to in situ ground-penetrating radar collected on-site in Greenland. “AR” refers exclusively to NASA Operation IceBridge airborne Accumulation Radar. The major high-level processing steps for each are shown in Supplementary Fig. 1, with implementation details in the remainder of the Supplement.



Supplementary Figure 1 | High-level processing steps for in-situ GPR and IceBridge AR data.
Orange lines depict GPR and AR upscaling and validation steps.

S.1. In situ GPR

S.1.1 GPR pre-processing

In situ GPR data was collected with a Malå 800 MHz shielded GPR Rx/Tx antenna collected with a mean spacing of 1.42 m between traces, resampled using a nearest-neighbour approach to constant 1.5 m spacing. In situ GPR transects were collected along a 1×1 km grid (50 m spacing)

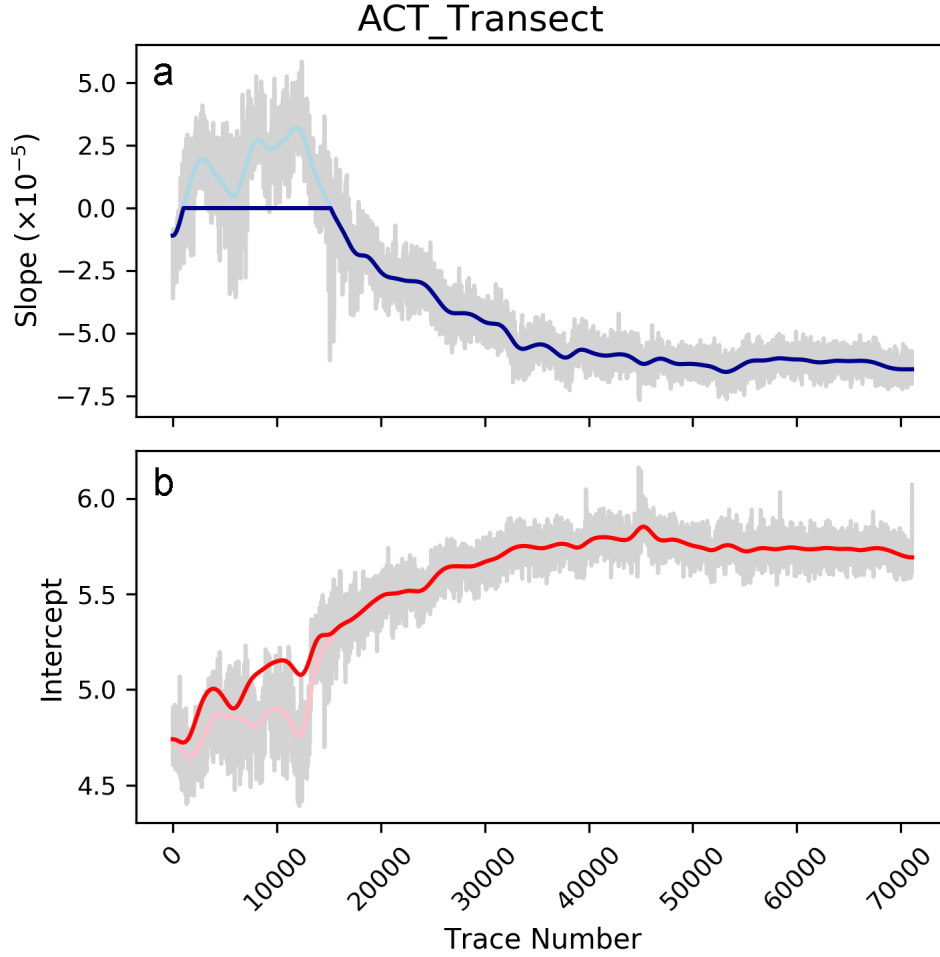
adjacent to Cores 1 and 2 and the KAN_U site, in select tracks near Cores 5 and 6 at Dye-2, and along the primary transect line adjacent to all of the remaining cores (Extended Data Fig. 2). GPR trace locations were recorded by a Trimble R7 global positioning system (GPS) receiver every 1 second. We applied a -1.35 m vertical offset and -3.65 m along-track horizontal offset to account for the difference between the GPS on the back of the snow machine and GPR antenna on the ground. GPR trace locations recorded between GPS-identified locations were linearly interpolated. We applied a de-wow filter to remove low-frequency artefacts and exponential gain filters to enhance the signal at depth. We combined individual GPR files along the main transect to form a single continuous transect.

S.1.2 Local log-variance calculations

A moving window spanning three traces horizontally (4.5 m) by thirteen samples vertically (1.3 ns, the span of one complete 800 MHz radar waveform) measured the variance of the signal in the 3x13 local neighbourhood surrounding each sample pixel. Thick ice slabs, having a homogeneous physical structure compared to surrounding firn, result in a lower local variance than samples within more porous and heterogeneous firn. GPR data were processed in their original 16-bit signed integer format as the gain/bias conversion from digital number to signal power would not enhance the signal further. We applied a \log_{10} -transformation to the GPR local variance data to linearize the data distribution.

S.1.3 Adaptive depth de-trending

After performing log-variance calculations, the variance of the signal still decayed with depth, especially in regions with primarily firn and little ice. The coherence of the GPR signal through firn decayed with depth much more quickly than through solid ice slabs. This vertical heteroscedasticity in the GPR data would cause false positive (Type-1) errors at depth if uncorrected. The remedy to the inconsistent signal decay in firn versus ice, we applied an adaptive vertical de-trending scheme to reduce Type-1 errors in firn. The algorithm calculated the linear vertical trend in the GPR data at each individual trace and smoothed the trends horizontally with a 1-km Gaussian filter, shown in Supplementary Fig. 2. In regions where the trend was negative and had a significant p-value < 0.05 , we corrected the linear trend to normalize the signal's strength with depth. Regions where the signal trends were positive with depth (the variance in the signal increased with depth) corresponded with areas where thick ice slabs were seen, indicating a "smooth" area within ice near the surface with "rougher" firn at depth. These areas remained unchanged.



Supplementary Figure 2 | Vertical slope and intercept of the log-variance of each GPR trace along the main GPR transect. 1 km Gaussian smoothing filters are shown in blue (for slope) and red (for intercept) both with and without omitting positive slope values.

S.1.4 Time-depth conversion

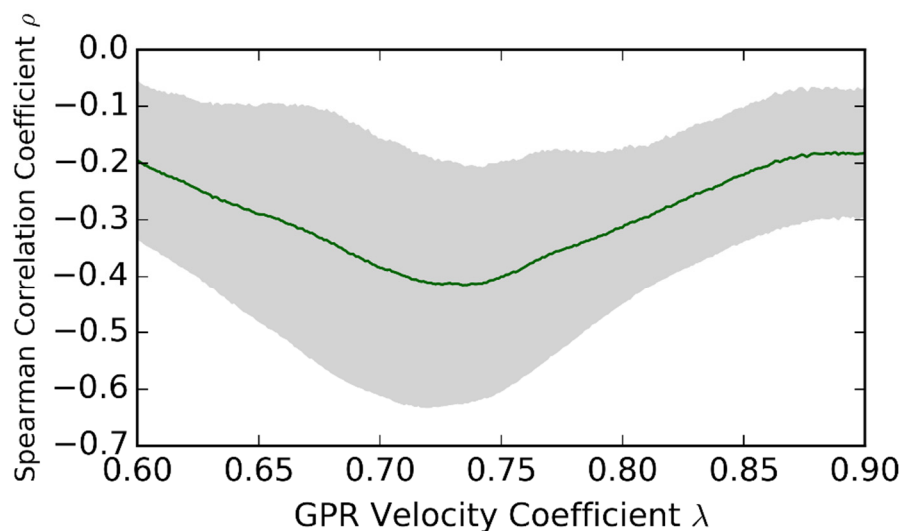
To calculate the speed of the GPR signal in firm, we used a the following formula previously postulated by Robin⁴⁷ and discussed later by Kovacs and others⁴⁸ to compute the dielectric constant ϵ'_r of firm with specific gravity ρ (a unitless measure of density) and a unitless empirical coefficient λ :

$$\epsilon'_r = (1 + \lambda\rho)^2 \quad (\text{S1})$$

We use the dielectric constant to convert two-way GPR travel time (t) to signal depth (D), (c = speed of light in a vacuum):

$$D = \frac{tc}{2\sqrt{\epsilon'_r}} \quad (\text{S2})$$

Robin empirically computed the value of the coefficient λ to be 0.851 (ref. 47), but Kovacs et al. showed this formulation produced dielectric constants that were too high tested against radar refraction sounding experiments⁴⁸. Using the cores 1-3 which contain ice slabs, we simulated the travel times through each core depth using λ values ranging from 0.60 to 0.90 at 0.01 increments, comparing them to the 10 nearest GPR traces to each core. We used a density of $877 \pm 25 \text{ kg m}^{-3}$ for the density of refrozen ice containing air bubbles, consistent with field observations⁵. We calculated a Spearman correlation between core density and GPR log-varianceⁱ. A λ value of 0.734 produced the strongest negative correlation between core specific gravity and GPR log-variance (Supplementary Fig. 3), providing the best local fit between the core densities and neighboring GPR traces. These values are consistent with the conclusions of Kovacs and others⁴⁸ and produce a GPR propagation speed of $182.4 \text{ m } \mu\text{s}^{-1}$ through refrozen ice within firm. We used this value to compute the depth and thickness of refrozen ice layers in GPR traces.



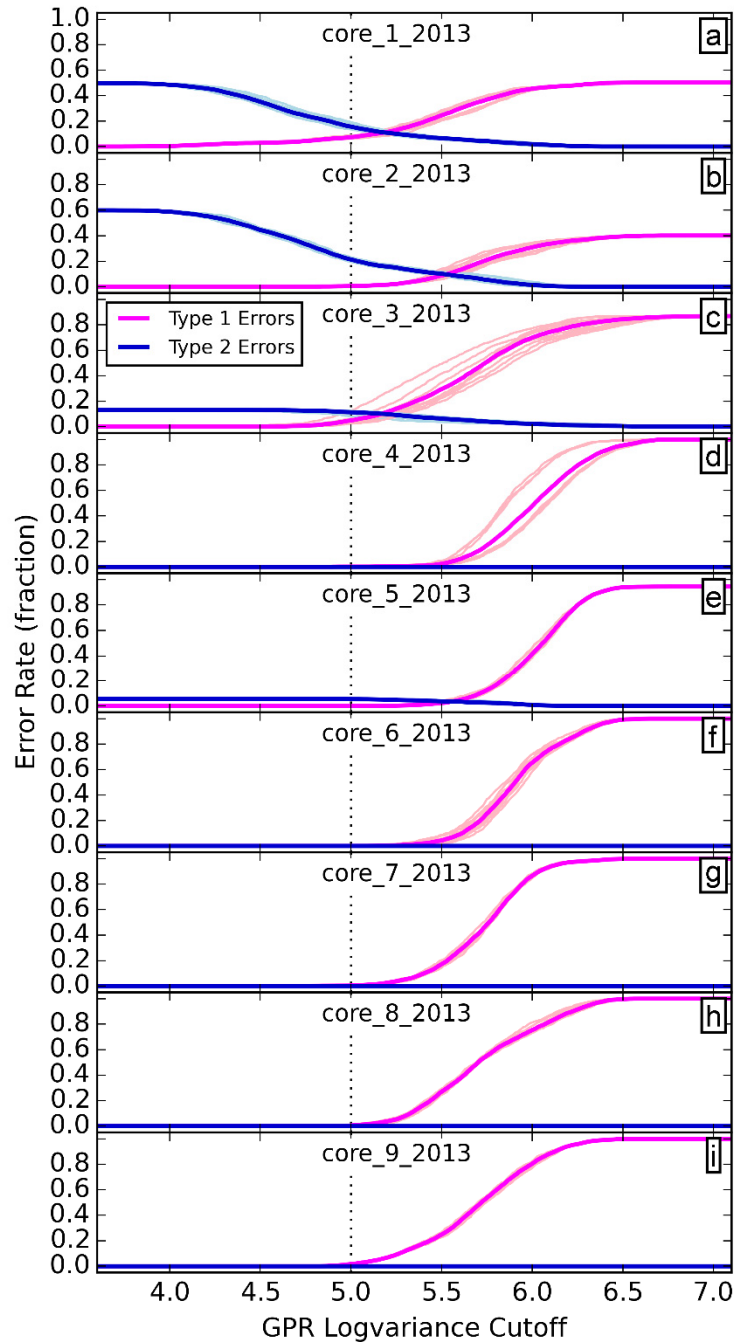
Supplementary Figure 3 | GPR velocity coefficients plotted against Spearman correlation coefficients between GPR signals & specific gravity of firn cores at equivalent computed depths.
Mean correlation is in green, standard deviation in grey.

S.1.5 Ice slab identification

A maximum local variance of 100,000 ($10^{5.0}$, 16-bit local neighbourhood digital-number signal variance) was chosen to identify ice layers, maximizing the agreement between GPR-detected ice slabs and those measured in nearby cores (Supplementary Fig. 4), looking only at ice volumes $\geq 50 \text{ cm}$ thick in the cores. If the GPR is converted to dB prior to processing ($dB = 20 \times \log_{10}(DN)$), this corresponds to a local variance of $\sim 408 \text{ dB}^2$, or a standard deviation of 20.2 dB within the local moving window. We chose this cutoff to minimize the occurrence of Type-1 (false positive) errors given an acceptable number of Type-2 (false negative) errors (Supplementary Fig. 4). Priority was given to minimizing Type-1 errors to avoid false positive selection of ice volume and provide a conservative estimate of ice extent. Given the size of the

ⁱ Spearman correlation coefficients offer slightly weaker values than traditional Pearson correlations, but do not rely upon the assumption of normalized data. Since neither our core densities nor GPR samples are normally distributed, we chose to use Spearman correlation rather than Pearson.

3x13 moving window, we can theoretically detect ice lenses ≥ 0.46 m thickness and spanning at least 9.0 m horizontal distance in the GPR, while thinner lenses which freeze heterogeneously in the firn¹⁰ are lost in processing. Ice layers < 1 m thickness were omitted from final results before comparison to IceBridge AR data.



Supplementary Figure 4 | Error distributions in each ACT-13 core as a function of GPR sensitivity cutoff. Type 1 (false positive) errors in magenta, Type 2 (false negative) errors in blue.

S.2 IceBridge Accumulation Radar Processing

We downloaded the Accumulation Radar³² (AR) dataset over the Arctic from 2010-2014 from the Center for the Remote Sensing of Ice Sheets (CRE SIS) FTP website³³.

S.2.1 IceBridge File Organization

We excluded AR files that lied entirely outside the boundaries of the Greenland ice sheet and peripheral glaciers according to the Greenland Ice Mapping Project (GIMP) mask³⁴. We excluded files that lied entirely in the Greenland's long-term ablation zone (where no firn exists), and in dry-snow and other areas of relatively little percolation (melt < 10 % of annual accumulation) where ice layers could not exist, and from high-accumulation regions with accumulation rates $\geq 1,000$ mm w.e. according to regional climate models, where high melt values are stored in perennial firn aquifers rather than refreezingⁱⁱ. Remaining files were manually filtered to eliminate files with poor data quality where no surface returns were identified or the data was of low-enough quality to not be usable.

After filtering, remaining AR files were grouped into "tracks," combining adjacent files in a single AR flight line to form continuous transects. We named tracks similar to the convention used in the original AR data: "YYYYMMDD_NN_AAA_BBB", where "YYYYMMDD" is the Gregorian calendar date of the AR flight line, "NN" is the identifier of that flight line in the day (typically "01", up to "05"), and "AAA" and "BBB" are the file numbers within that flight line. Tracks ranged in length from 1 AR file to 17 files, spanning between 19.5 and 367 km in length per track. The entire dataset contains 320 tracks consisting of 892 original AR files. The tracks overfly a total 19,096 km of Greenland's lower accumulation zone. We applied a \log_{10} transformation to the AR track files to convert to decibels. This log-transformed data was used for the remainder of processing.

S.2.2 Surface picking and filtering

AR files contain auto-selected surface returns in the radar signal. Although many of these auto-picked returns are sufficient to visually inspect the data, a significant number of artefacts and incorrectly-identified surfaces remained in the provided data.

We improved selection of the "true" physical surface using two assumptions. First, the radar signal at the surface is a very bright reflector compared to the relatively weak atmospheric returns and the firn at depth. Second, the surface of the ice sheet in the interior accumulation zone is relatively smooth, and does not contain large jumps in elevation between individual traces.

Beginning with the auto-selected "surface" return at the first trace in each AR track, we use a vertical "search window" spanning 50 pixels above and below that value. By visual inspection, we found the true physical surface was within this search window of the first trace in all but eight (8) of the AR tracks. In these eight tracks, we hand-selected initial "suggestions" for sample numbers within the file in order to begin searching for the surface (Supplementary Table 1).

ⁱⁱ The accumulation cutoff delineating ice slabs from firn aquifer regions was later found to be 572 mm w.e. annual accumulation, as explained in the main text. 1000 mm w.e. was used as an initial value for filtering files.

Supplementary Table 1 | Suggested vertical pixel locations for surface searching in AR tracks where the auto-picker was unsuccessful in identifying the initial surface.

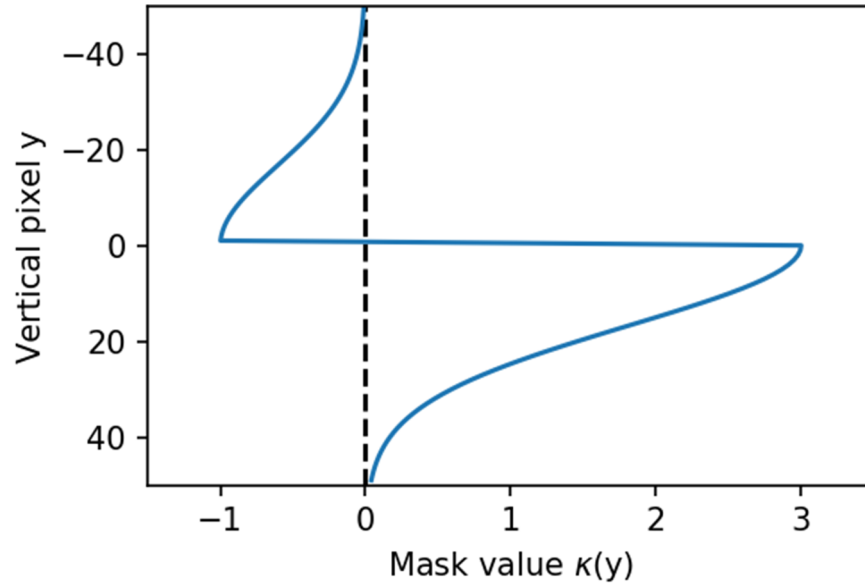
AR track name	Suggested starting surface, vertical pixel location
20120330_01_025_026	2,936
20130419_01_004_005	1,850
20130423_01_002_003	1,426
20130423_01_069_069	1,678
20130423_01_125_125	1,755
20130423_01_127_127	1,676
20130423_01_130_132	1,623
20130426_01_006_007	2,234

Using a vertical pixel range of y-values of $[-50, 50]$, a 3-standard-deviation pseudo-Gaussian kernel $\kappa(y)$ was created using the following modified Gaussian formula (Equations S3-S4, Supplementary Fig. 5). This kernel, when multiplied over 100 vertical pixels in the AR and summed, would reach its maximum value when centered over the “bright” reflection from the surface (with dark atmosphere above and dimming surface returns at depth).

$$\kappa(y) = e^{\left[\frac{(y-\mu)^2}{2} \right]} \times S(y) \quad (S3)$$

$$S(y) = \begin{cases} -1, & y < 0 \\ +3, & y \geq 0 \end{cases} \quad (S4)$$

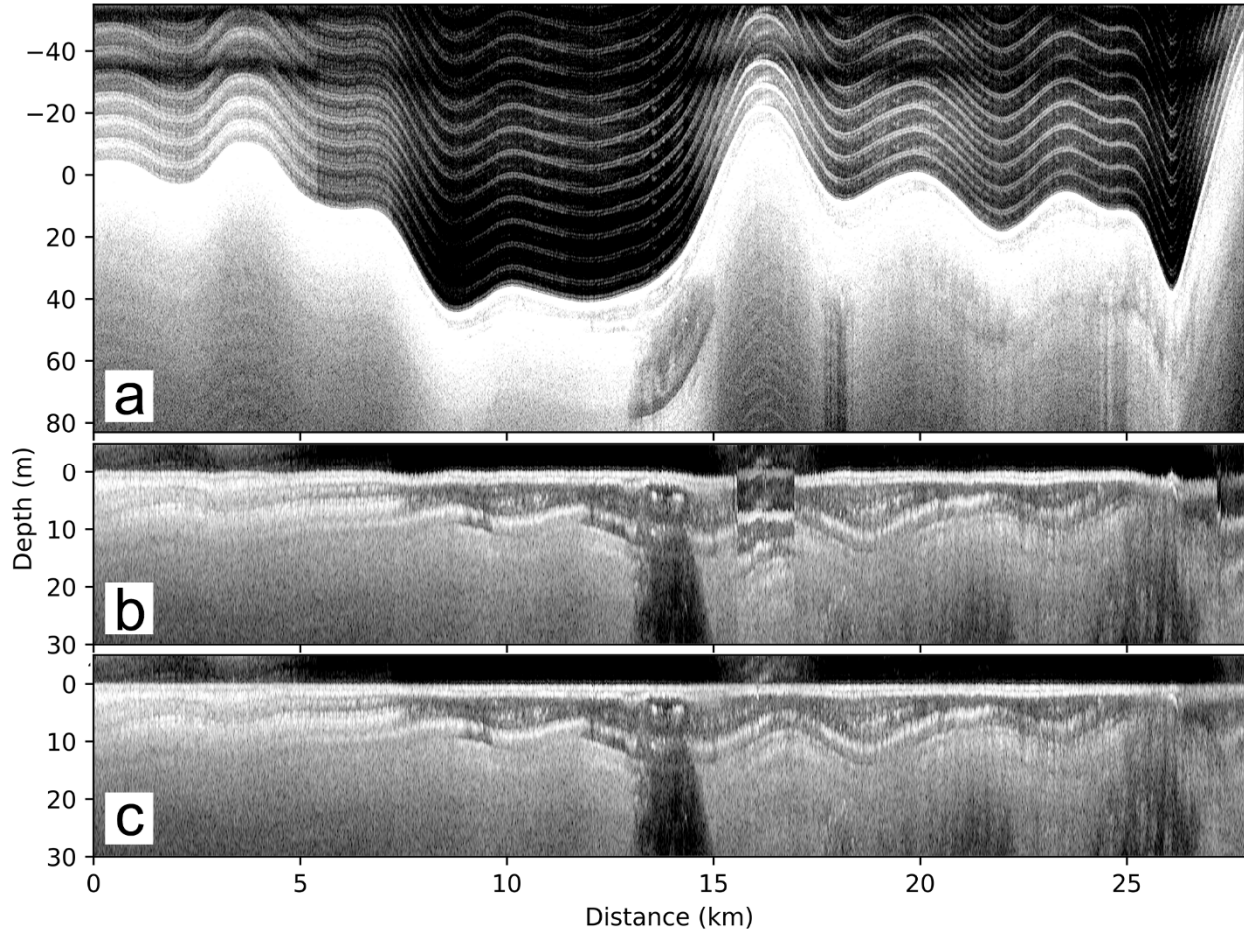
$$y = [-50, 50], \sigma = \frac{50}{3}, \mu = 0$$



Supplementary Figure 5 | Surface-identifying kernel used for selecting the ice sheet surface.

The mask kernel $\kappa(y)$ was multiplied by the vertical return strengths in a ± 50 pixel moving window for ± 150 pixel search radius above and below the initial suggested surface pixel. The highest value within that window was chosen as the surface. Relying upon the second assumption of relative surface continuity, the search window for the next surface trace was centered at the previous selected surface location, with the process repeated until the end of the track.

The mask kernel successfully picked the surface in the majority (>99 %) of AR traces. Some AR files contained significant echoes in the AR data (Supplementary Fig. 6a), and the selections using the kernel caused a “choppy” uneven surface (Supplementary Fig. 6b), which violates the second assumption described above. Jump artefacts were typically short-lived (<20 traces) before returning to the correct surface. To automatically detect where jumps occurred, we calculated the linear slope of the surface in the 10 traces (~ 200 m) preceding each individual trace and calculated whether the surface slope to the next trace was more than 5 vertical pixels (1.5-2.5 m) above or below what would be expected if the surface trend continued along the same slope as before. We looked ahead, up to 20 pixels, to find an identified surface whose elevation was consistent within ± 10 % with of the prior slope. If we found such a pixel, we linearly interpolated over the gap. Approximately 0.72% of surface traces pixels were corrected in this manner.



Supplementary Figure 6 | Surface picking example on IceBridge track 20110329_04_001_002. (a) Raw data with undulating surface and visible radar echoes. (b) AR surface using automated surface picks as provided with AR data. (c) Improved surface picks using mask thresholding and surface-continuity corrections.

AR tracks were visually inspected to ensure the automated surface picks provided reasonable surfaces. Remaining artifacts were identified and masked out from further processing, in which 0.38 % of all remaining AR traces were omitted.

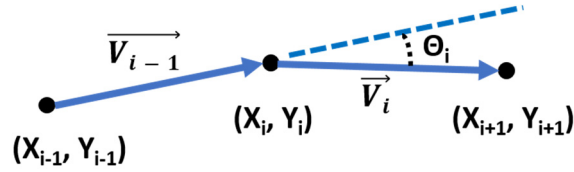
S.2.3 Roll Correction

IceBridge AR returns are affected by roll of the aircraft, when the instrument is pointed off-nadir the returns are inherently weakened, at times significantly. We used a correlation between near-surface return strength and aircraft roll to correct the AR data for aircraft roll.

S.2.3.1 Roll vs path curvature correlation

In most years of IceBridge AR collection, the horizontal roll of the aircraft is included with each AR trace. In one year (2012) aircraft roll data was omitted from AR files. To account for this missing data field, curvature of the flight path was substituted for roll of the aircraft on the assumption that the aircraft is tilted left when the aircraft is physically turning left, and vice-versa when turning right. Path curvature was computed from the coordinates of each AR trace

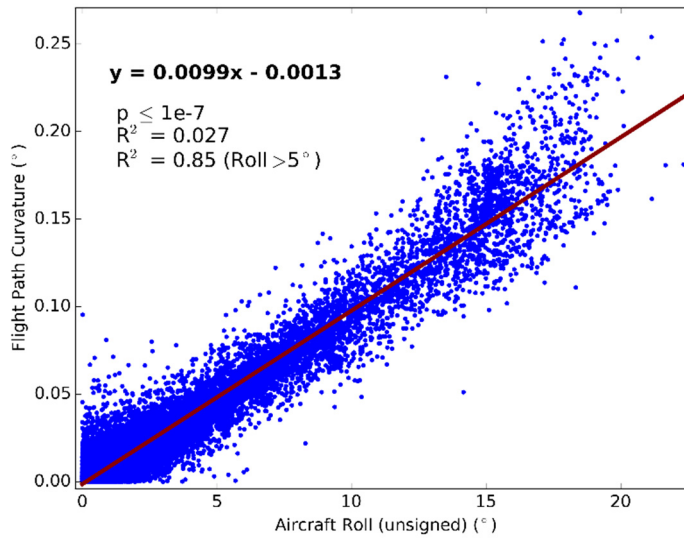
using vector algebra. Trace locations were converted to WGS 84 / NSIDC North Polar Stereographic Projection (EPSG: 3413), and vectors V_i were computed between each trace (Supplementary Fig. 7 and Equations S5 and S6):



Supplementary Figure 7 | Schematic diagram for computing aircraft path curvature.

$$\vec{V}_i = (X_{i+1} - X_i, Y_{i+1} - Y_i) \quad (S5)$$

$$\theta_i = \cos^{-1} \left(\frac{\vec{V}_{i-1} \cdot \vec{V}_i}{|\vec{V}_{i-1}| * |\vec{V}_i|} \right) \quad (S6)$$



Supplementary Figure 8 | Correlation between aircraft roll and aircraft path curvature.

IceBridge AR signal strength is weakened most when the roll of the aircraft is greater than 5° . The correlation between aircraft roll and path curvature is high ($R^2 = 0.85$, $p \leq 10^{-7}$) when roll values are greater than 5° (Supplementary Fig. 8). In regions of low roll ($\leq 5^\circ$) the two variables show little correlation. Signal strength is minimally affected when the aircraft roll is low and little if any correction is needed. In years when aircraft roll was unavailable (2012), path curvature was substituted. Since roll corrections are computed separately for each flight line, it was not necessary to explicitly convert between the two.

S.2.3.2 – Depth-dependent roll correction

Aircraft roll (especially above 5°) causes off-nadir reflections of the AR signal and weakens the returned signal. The magnitude of this weakening depends upon aircraft altitude, elevation, initial signal strength, aircraft and instrument configurations. All of these factors vary between years of the IceBridge mission and even between individual flight lines. To correct for this effect, we compute roll-dependent signal strength on each flight line individually.

Additionally, a roll-dependent weakening of the signal depends upon depth below the physical surface. Radar returns become weaker at depth regardless of aircraft roll. We performed a depth-dependent roll-correction to accurately normalize the GPR data and negate roll-dependent weakening of the signal.

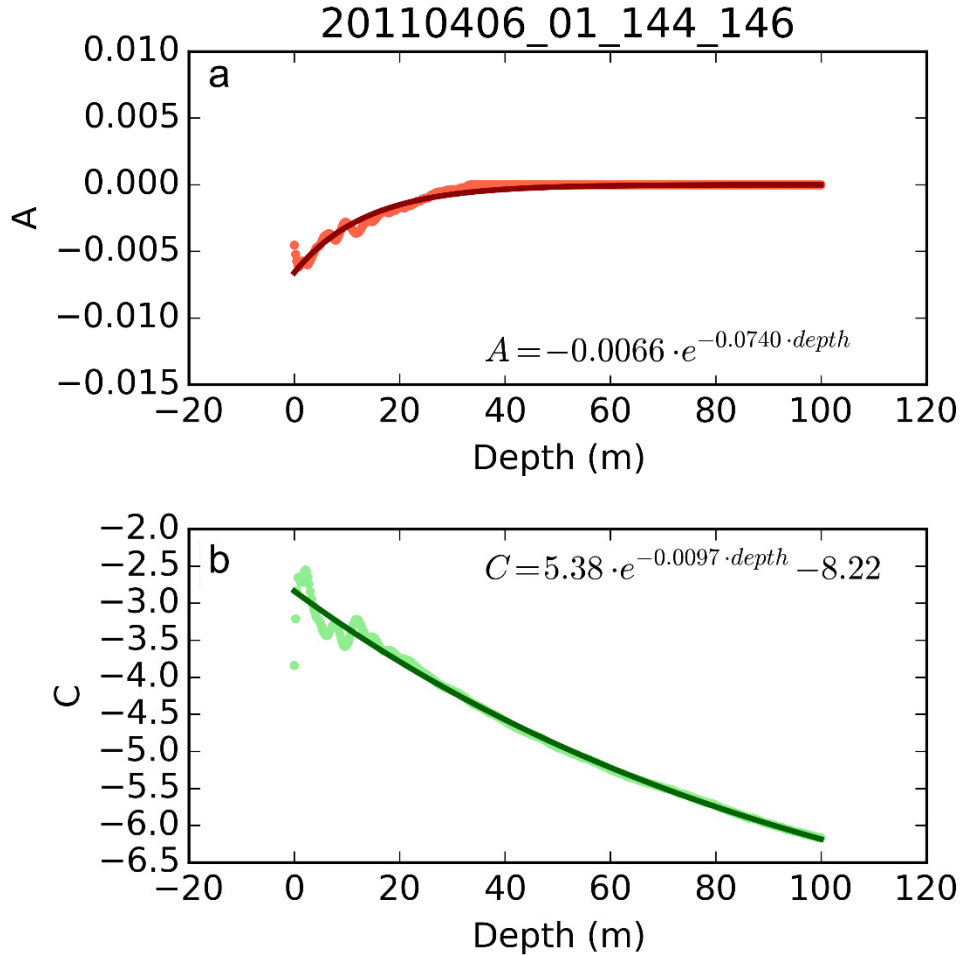
We calculated the signal strength through the top 100 meters of firn/ice in each flight line, plotted against the roll of the aircraft (or path curvature when the roll wasn't available). Aircraft roll (Θ) typically varied between 0 and 20°, affecting signal strength (Ω) approximately quadratically, with empirically-derived factors A and C:

$$\Omega(\theta, y) = A(y) \cdot \theta^2 + C(y) \quad (S7)$$

We varied the values of A and C with depth using exponential decay functions. A(y) approaches zero at depth and C(y) converges on a single average value, making $\Omega(y, \Theta)$ approach a constant function (with no correction applied to the signal) at depth. For each flight line, the functions A(y) and C(y) are independently computed as a function of depth (y), in meters:

$$A(y) = R e^{-S y} \quad (S8)$$

$$C(y) = T e^{U y} + V \quad (S9)$$



Supplementary Figure 9 | Depth-dependent roll functions $A(y)$ and $C(y)$ for flight line 20110406_01_144_146. (a) $A(y)$ and (b) $C(y)$ with best-fit curves for equations S8 & S9 plotted on top.

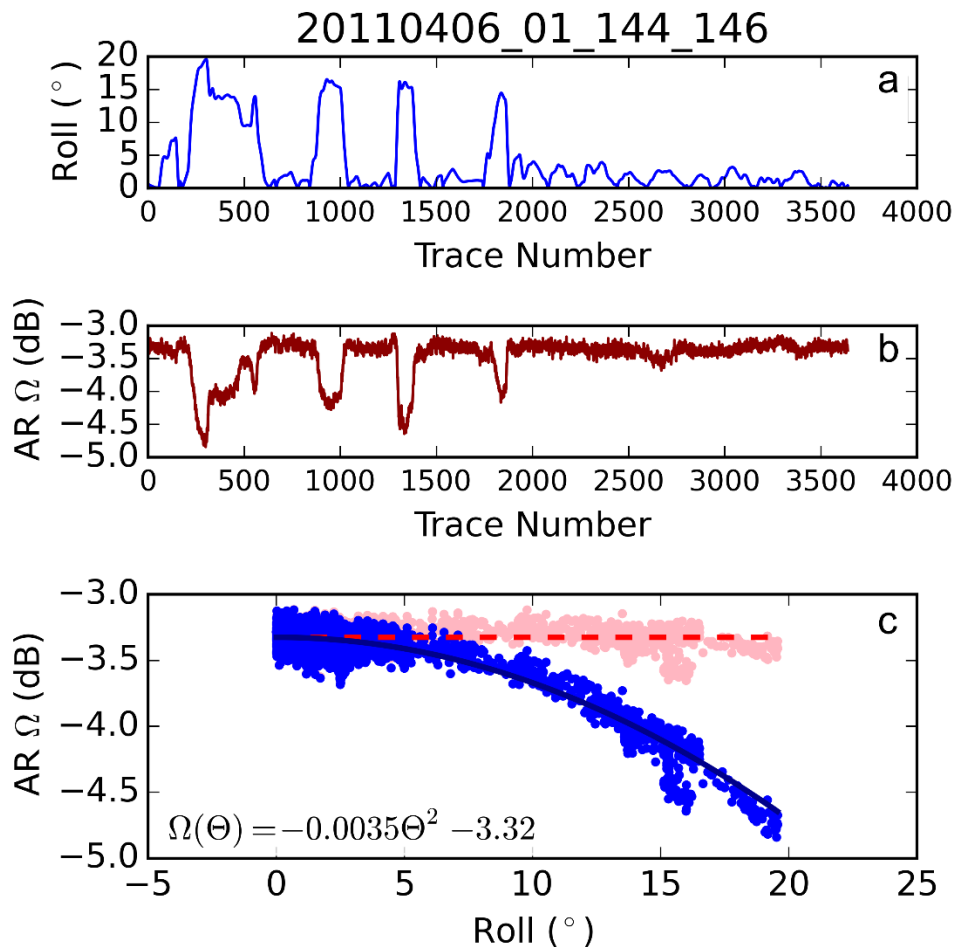
We use least-squares curve-fitting to compute $A(y)$ and $C(y)$ and provide the best-fit $\Omega(y, \Theta)$ function at each depth (Supplementary Fig. 9 for track “20110406_01_144_146”). The empirical factors R, S, T, U and V used for every IceBridge AR track are located in the “Supplementary_Table_3.csv” text file accompanying this supplement.

Mean R^2 fits for tracks with rolls $>5^\circ$ were 0.67 ± 0.31 and 0.98 ± 0.010 for the functions $A(y)$ and $C(y)$, respectively, with mean p-values of 0.048 ± 0.17 and $\sim 1e-7 \pm 1e-8$ (1 SD), respectively. In flight lines where the p-values for the $A(y)$ curve were statistically insignificant (>0.05), the best-fit function $A(y)$ trended extremely close to zero, which caused the GPR data in traces with roll $>5^\circ$ roll to be adjusted by less than one percent ($0.65 \pm 1.04\%$, 1 SD). Areas with roll $<5\%$ were adjusted minimally ($\ll 0.1\%$). AR tracks with aircraft roll values $>5^\circ$ consistently resulted in curve-fit functions $A(y)$ and $C(y)$ with statistically significant fits ($p < 0.05$), enhancing the AR signals in regions with $>5^\circ$ roll by $5.95 \pm 5.67\%$ (1 SD).

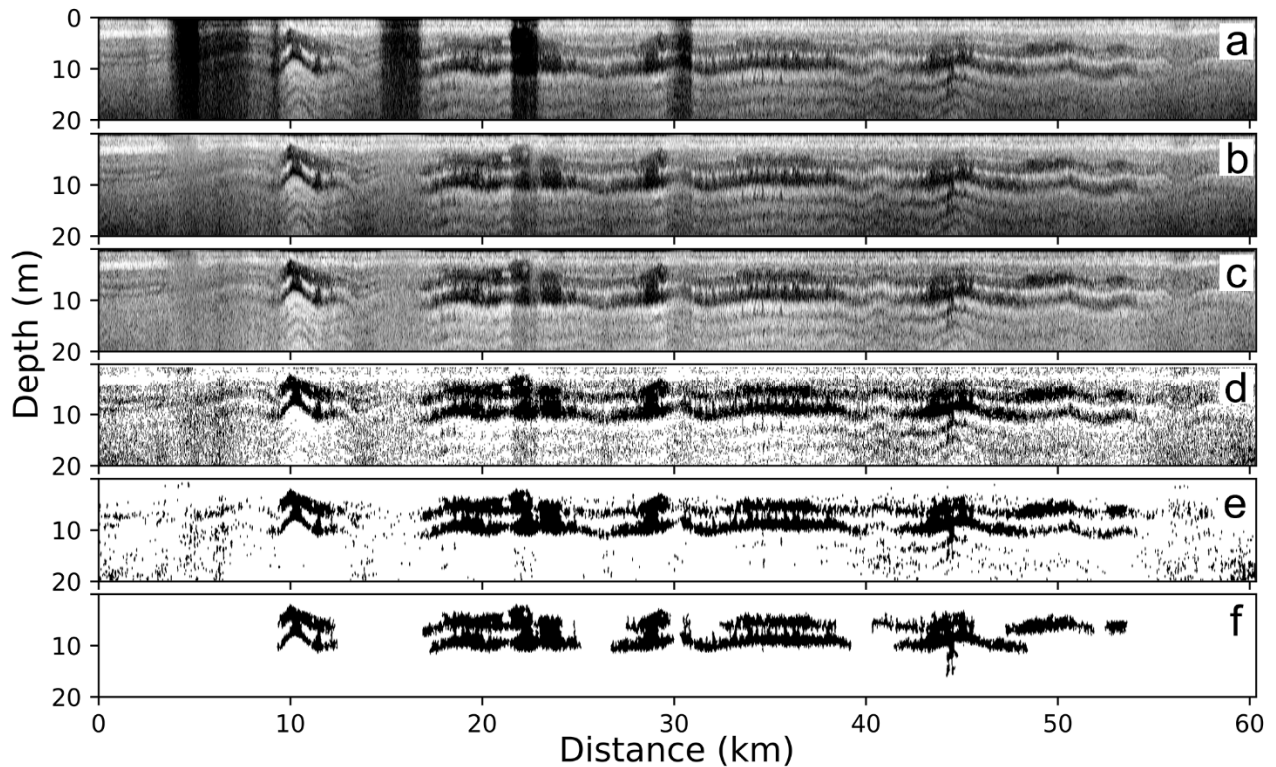
We use the functions $A(y)$ and $C(y)$ calculated in equations S8 and S9 to convert raw AR samples (Ω_{raw}) to roll-corrected samples ($\Omega_{corrected}$):

$$\Omega_{corrected}(\Theta, y) = \Omega_{raw} \cdot \frac{C(y)}{A(y) \cdot \Theta^2 + C(y)} \quad (S10)$$

When roll (Θ) is zero, traces are multiplied by 1.0 (not adjusted). Since $A(y)$ and $C(y)$ are negative, adjustments increase with aircraft roll (Θ). The adjustment asymptotically decays to 1.0 at greater depth (y), providing less adjustment to the weaker signals at depth where the signal is less affected by aircraft roll. Supplementary Fig. 10 illustrates for the same flight line 20110406_01_144_146, which includes several instances when the aircraft turns and rolls by 15-20°.



Supplementary Figure 10 | Example of roll corrections on IceBridge flight line 20110406_01_144_146. (a) Roll of the aircraft. (b) Average AR signal strength within the top 20 meters of firn along the same line. (c) Aircraft roll versus mean signal strength of the top 20 meters firn, with quadratic trend lines through the pre-corrected traces (blue) and post-corrected traces (red). The inset formula shows the mean A and C parameters computed for the top 20 meters of firn (Equation S7).



Supplementary Figure 11 | Processing steps of flight line 20110406_01_144_146. (a) After surface picking, before correcting for aircraft roll, (b) after correcting for aircraft roll, (c) after correcting for depth attenuation, (d) after initial thresholding to identify dark regions of the image, (e) after initial noise filtering, and (f) after isolating large continuous segments of ≥ 350 pixels. The dark regions in panel F are identified as ice slabs.

Supplementary Fig. 11, panels a and b, illustrate the effect of roll-correction on the AR data. Roll corrections were applied to each flight line individually. When aircraft roll is minimal ($\leq 5^\circ$), flight lines were adjusted only slightly, by an average factor of $0.30\% \pm 0.52\%$ (1 SD). Regions where aircraft roll was greater than 5° were strengthened by a mean factor of $5.5\% \pm 5.6\%$ (1 SD).

S.2.4 – Removing lakes and other radar artifacts

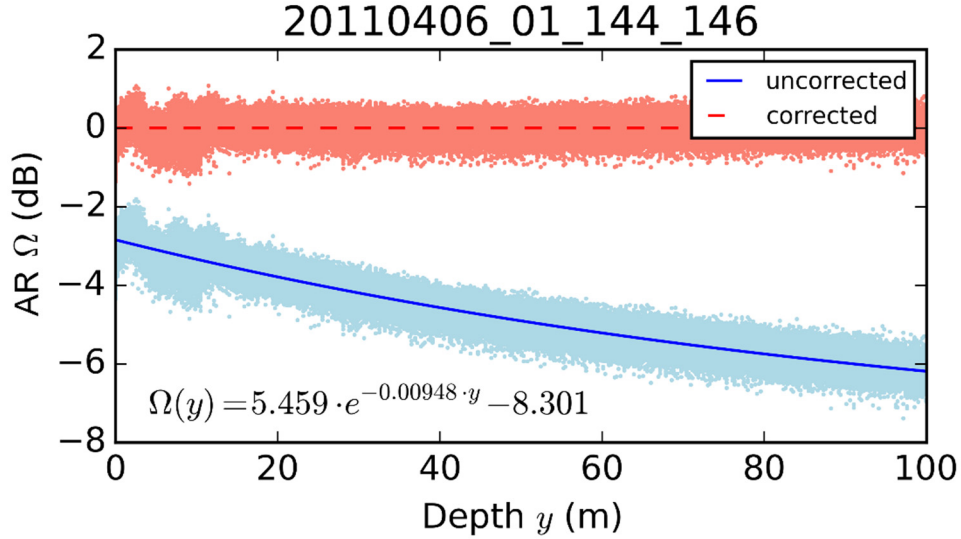
Surface lakes that remain unfrozen through the winter, as well as perennial firn aquifers, create anomalous radar backscatter signatures, which appear in the IceBridge AR data as extremely bright shallow reflectors (≤ 10 m depth) with a rapid extinction of the signal to depth³⁵. To correct the AR signals for depth, 113 instances of lakes and/or aquifers in the AR data were hand-picked and removed from the flight lines in further processing steps. Additionally, we selected a small number of anomalously weak signals ($< 0.1\%$ of the data), the primary causes for which were not identified, and removed them from the data set to provide consistent returns.

S.2.5 Depth Correction and Normalization

AR return signals in firn and ice get weaker with depth, consistent with Beer's Law for electromagnetic waves propagating through an attenuating medium⁴⁹. To homogenize the radar

signal with respect to depth, we fit a scatterplot of the top 100 meters in each flight line to an exponential decay curve (Supplementary Fig. 12):

$$\Omega(y) = Ae^{By} + C \quad (S11)$$



Supplementary Figure 12 | Depth-correction curve fit, correction and normalization results on AR flight line 20110406_01_144_146.

Factors B and C are both constrained to be negative, and each AR flight line is then corrected for depth using the least-squares best-fit values for A, B and C from Equation S11,

$$\Omega_{depth_normalized}(y) = \frac{\Omega(y) - C}{A} - e^{-By} \quad (S12)$$

where y is signal depth (meters) and $\Omega(y)$ is the mean strength of the signal along the flight line at that depth.

Additionally, we subtracted the mean value of the AR data in each flight line, centering the data on zero, and divided by the standard deviation to normalize each flight line to a consistent scale of return strengths with a mean of zero and a standard deviation of one, allowing us to further process the data consistently across all IceBridge AR tracks. The effects of this depth-correction and normalization are illustrated in Supplementary Fig. 11 c and Supplementary Fig. 12.

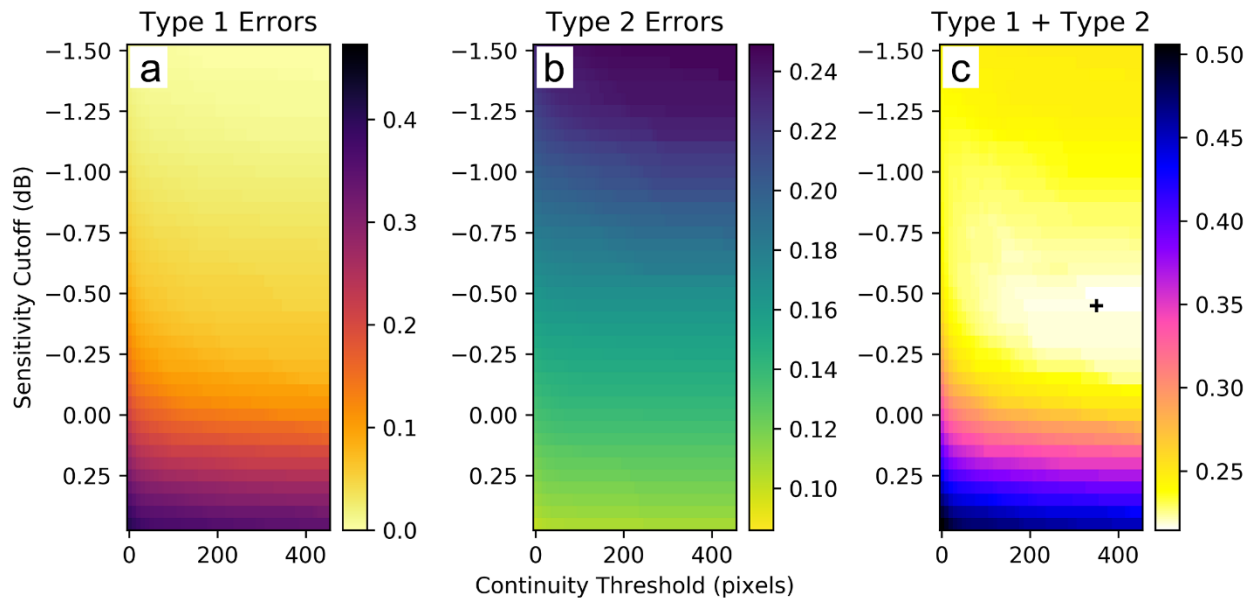
S.2.6 Thresholding and Continuity Filtering

After correcting AR data for aircraft roll, penetration depth and removing anomalous artifacts such as lakes, we selected thick ice layers in the data. The relatively low resolution of the AR data (approximately 20 m horizontally and 0.25-0.50 m vertically) prevents adopting a “local variance” technique used in the higher-resolution in situ GPR (Section S.1.2). The AR radar scatters less in solid ice slabs than in more porous firn. In the presence of refrozen ice layers >2 times the vertical resolution of the radar (approximately 1 m and greater), it is possible to pick out ice slabs from return strength alone, as long as the ice slab is both thick and continuous enough to distinctly classify against background noise.

We resample the in situ GPR processed in Section S.1 to the same grid-spacing as the IceBridge AR reference track “20130409_01_010_012,” which was flown 3 weeks prior to the in situ radar on the same line. The AR flight line and the in situ GPR are separated by an average of 17 m, with 99% of the in situ radar signals falling within 150 meters cross-track distance from the AR flight line. Each pixel in the down-sampled in situ track was assigned a boolean value (“ice” or “no ice”) based on a majority of in situ pixels that fell within it. If $\geq 50\%$ of the original pixels within the down-sampled pixel contained ice, the down-sampled pixel was identified as containing ice, and vice-versa. We use this “idealized” down-sampled in situ radar dataset to validate the IceBridge AR flight line.

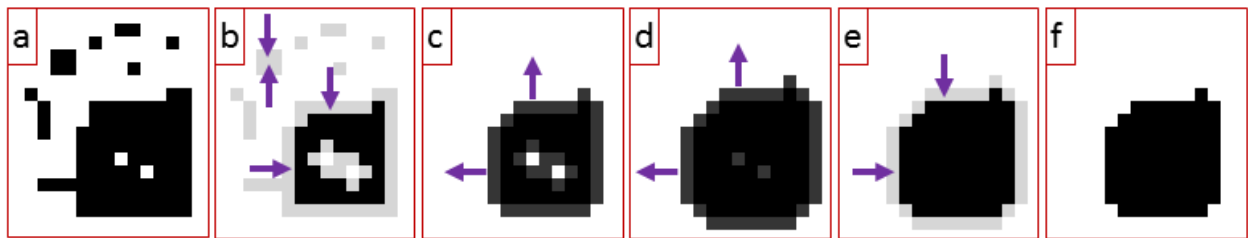
Normalized AR data contains values centered at zero with a standard deviation of one, and ice slabs appear generally darker (weaker return values) than areas of snow and porous firn. We use a three-step process to convert normalized IceBridge AR data into boolean (“ice”/“no ice”) values. First, we identify all “weak” pixels with signal strength beneath a sensitivity cutoff value (Supplementary Fig. 11d). We then use a simple image-processing technique to filter out small-scale noise from the data, 1-2 pixels wide (Supplementary Fig. 11e). Knowing that ice slabs are both thick and relatively continuous (extending for kilometers), we then apply a “continuity threshold” to only choose regions of the image that are spatially connected to other identified pixels for N continuous pixels (Supplementary Fig. 11f).

We first selected ice values within the IceBridge reference track using a range of 41 sensitivity cutoffs (-1.5 to +0.5, by 0.05) and 46 continuity filter cutoffs (0 to 450 pixels, by 10) and measured the false positive (Type-1) and false-negative (Type-2) errors against the down-sampled in situ GPR (Supplementary Fig. 13). The minimum error of 0.214 is reached when using a normalized GPR sensitivity cutoff of -0.45 dB and continuity cutoff of 350 pixels. This gives the IceBridge AR processing an error rate of -16.5% to +4.95% for identifying ice slabs, compared to the in situ GPR.



Supplementary Figure 13 | IceBridge AR reference track 2013040901_010_012 error rates compared with resampled in situ GPR as a function of continuity thresholds and radar sensitivity cutoffs. (a) Type 1 errors, (b) Type 2 errors, and (c) combined errors (Type 1 + Type 2). The minimum combined error value of 0.214 at (350, -0.45) is identified in panel (c).

In each run of the error-minimization search outlined above (Supplementary Fig. 13), after applying the sensitivity cutoff and before applying the continuity cutoff, we use a simple image-processing technique to filter out small-scale noise 1-2 pixels in diameter. The majority of IceBridge AR noise-pixels falls into this category (Supplementary Fig. 11d), and the “shrink and grow” method removes the majority of this small-scale noise (Supplementary Fig. 14).

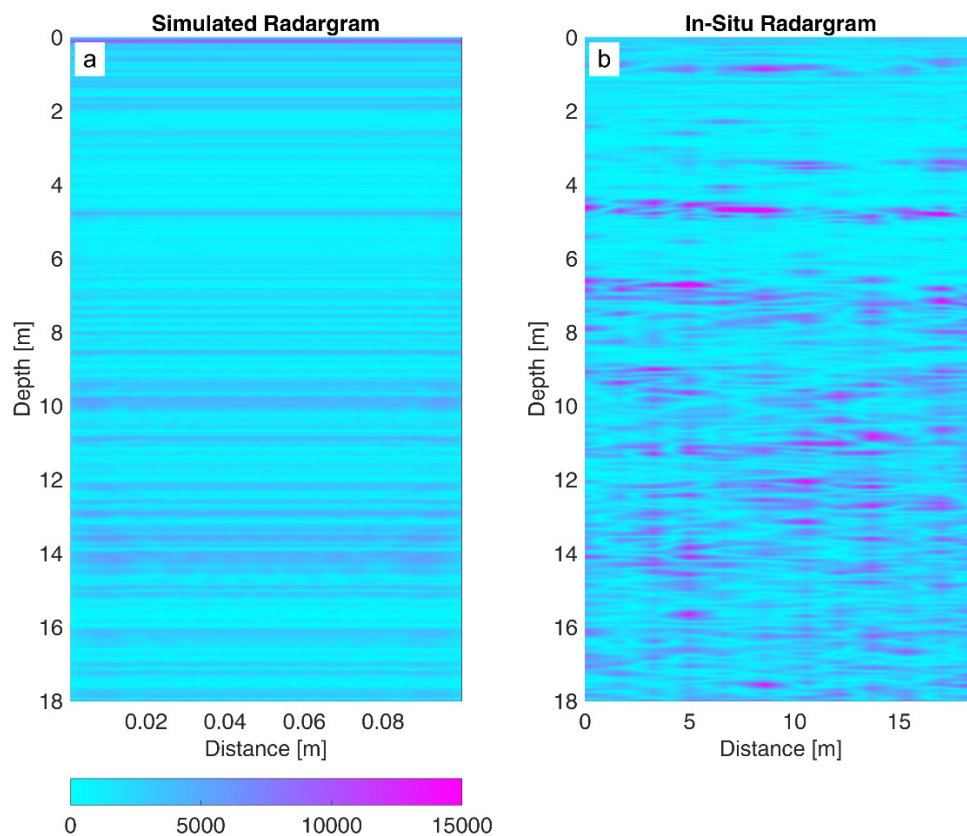


Supplementary Figure 14 | Schematic illustration of small-scale noise filtering algorithm. (a) The original picture with noise, (b) shrink edges by 1 pixel to eliminate single-pixel assignments, (c) re-grow edges by 1 pixel to their original size, (d) grow edges by one pixel to eliminate single-pixel omissions, (e) shrink pixels back to original size, (f) final product, with 1-2 pixel-width noise removed.

S.3 GPR Empirical Modeling Validation

The algorithms described above use an empirical approach to correct for noise, attenuation, and non-signal scattering. Such an approach was necessary given the wide range of platforms, aircraft, and antenna configurations on NASA’s Operation IceBridge missions. In case the radar wavelength of the applied antenna system is shorter than the reflecting object or larger than the interface roughness of reflecting surfaces, modeling of GPR refraction and reflection is applicable to identify possible sources of reflection responses. However, the consideration of all

types of subsurface in-homogeneities is practically impossible⁵⁰. To validate the GPR and AR data against more physically-based approaches, we have applied a finite-difference time-domain (FD-TD) model to GPR radar at the KAN_U site to generate synthetic high-resolution radargrams to compare with empirical results. Considering just air and ice as contributing volume fractions, scattering can be directly related to the near-surface firn stratigraphy, using densities from adjacent cores⁵¹. We used in situ determined firn densities measured in cores as input data to simulate radar responses. The available vertical resolution in density was limited to 0.1 m. Since all cores were drilled in dry conditions (snow and firn temperatures far below 0 °C), we can convert density to relative dielectric permittivity⁵². The simulated radargram (for a core diameter of roughly 0.09 m) is compared with in situ radar traces being recorded within a 10m radius to the core location (Supplementary Fig. 15 and Extended Data Fig. 2). We applied the post-processing radar algorithm described in section S.1.2 Local log-variance calculations and analyzed for ice slab occurrences. The exact thicknesses of ice slabs differed slightly at higher resolutions, but when using an enlarged variance window to cover the same physical distance and depth used previously by the algorithm, we found ice slabs were accurately detected with a 94% overlap compared to the empirical algorithm described previously. Although exact details differed between the two outputs, we did not see significant differences in overall ice slab thickness or location (Supplementary Fig. 15).



Supplementary Figure 15 | Finite-Difference Time Domain models of the 800 MHz radar signal. (a)

For a single core of the GPR transect. (b) FD-TD model on an up-sampled ~18 m segment of the GPR transect simulating firn variability from original GPR traces nearest to Core_2013_1 (Extended Data Fig. 1). Color scale refers to modeled values of relative simulated signal strength (unitless). Ice slabs exist in the smooth areas in the top 6.5 m of the radargram.

Scattering produced by surface roughness or inhomogeneous geometries in the subsurface is very consistent for different ice facies at Devon Ice Cap⁵¹, similar to the ones observed in this study. We conclude that snow and firn stratigraphy are the dominating source of radar scattering for airborne and ground based investigations. We ran the AR processing algorithms on 2 flight lines over known dry-snow locations where coincident validation cores are available³¹ at Summit (72.57742 °N, 38.46955 °W) and EastGrip (75.62518 °N, 35.97873 °W). At each site, small ice lenses (1-2 cm) are present from the anomalous 2012 melt season⁷, but no thick ice slabs exist. Noise pixels were not contiguous enough to pass the continuity threshold described in Section S2.6, and were not identified as ice slabs by our algorithm (see noise in Supplementary Fig. 11e-f for illustration). Results support that only thick and continuous stratigraphic features with high homogeneity relative to firn, and low radar backscatter, are detected by the applied algorithm at locations where they physically occur.

S.4 Mapping Ice Slabs

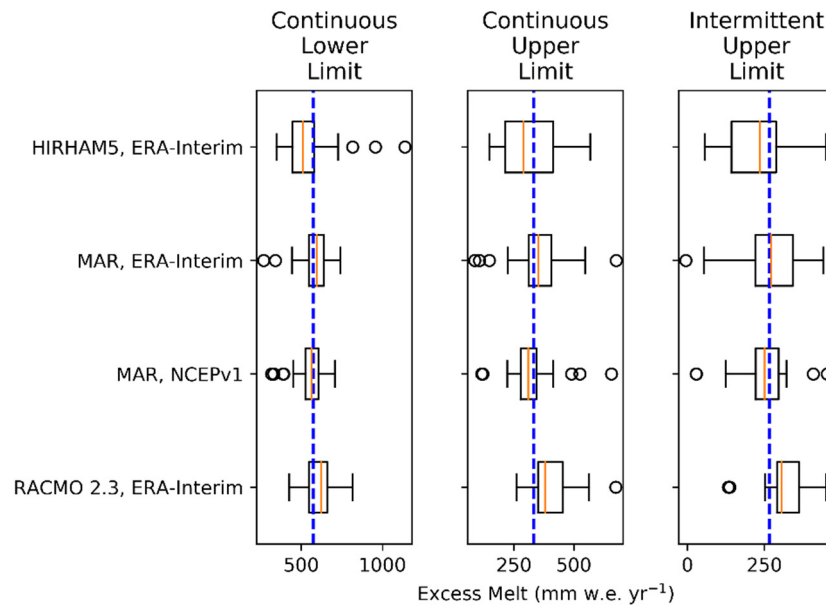
We use Regional Climate Models (RCMs) forced by reanalysis data to assess the conditions under which recent climate has formed these ice slabs (main text, Table 1). To compute the thresholds of excess melt which have cause ice slabs to form thick enough to reliably detect with airborne radar, we selected 44 IceBridge transect lines (Supplementary Table 2) that are oriented “uphill” or “downhill” and lay approximately perpendicular to the length of ice slabs areas (Fig. 2).

Supplementary Table 2 | AR tracks used in cross-track Excess Melt thresholding

20100507	04	070	070
20100508	01	114	115
20100510	01	034	041
20100515	01	007	009
20100519	01	036	036
20100519	01	048	050
20100519	01	057	058
20100519	01	069	069
20110329	04	001	002
20110329	05	001	002
20110331	01	043	044
20110412	01	158	160
20110414	01	004	007
20110418	01	016	017
20110418	01	173	175
20110423	01	072	074
20110423	01	078	080
20110425	01	011	013
20110516	01	042	044
20120412	01	095	095
20120414	01	005	007
20120416	01	004	005
20120416	02	117	119
20120417	01	073	075
20120418	01	005	007
20120419	01	011	013
20120423	01	006	007
20130405	01	011	013
20130408	01	009	021
20130409	01	010	012
20130409	01	131	133
20130411	01	009	010
20130411	01	164	166
20130415	01	015	017
20130415	03	033	034
20130423	01	002	003
20140408	04	001	003
20140416	04	024	027
20140416	05	007	009
20140416	05	035	037
20140419	03	034	035
20140419	03	048	048
20140508	02	019	020

Using these transects we define three thresholds: a lowest extent of “continuous” ice slabs (highest mean excess melt at the lowest-elevation portion of the ice slab), the upper extent of “continuous” ice slabs (where ice slabs begin to have detected “gaps” that are wider than the ice slab spans on either side of them), and an upper extent of “intermittent” ice slabs (lowest mean excess melt, at the most uphill extent, in which ice slabs stop being detected at all, regardless of gaps between them).

The excess melt values for ten year running preceding the IceBridge AR measurements show a good agreement between different RCMs (Supplementary Fig. 16), with the inter-quartile ranges overlapping among nearly all of the different RCMs. We selected the mean values of 573.1, 332.7, and 266.0 mm w.e. as the Lower Continuous, Upper Continuous, and Upper Intermittent values of melt that cause ice slabs to appear, respectively. The total extent of detected ice slabs appear between the upper intermittent and lower-continuous values, or 266 – 573 mm w.e. for a decade or more, respectively. Detection of continuous ice slabs (between the Continuous Lower and Continuous Upper limits) were used to constrain areas that would affect runoff. Intermittent, topographically-dependent slabs could affect runoff locally on km scales but would not likely cause runoff from the ice sheet, and were considered when calculating runoff from the ice sheet.



Supplementary Figure 16 | Excess Melt threshold distributions for the Continuous Lower, Continuous Upper and Intermittent Upper extents of known ice slabs detected in IceBridge radar. Orange lines are medians, boxes are the inter-quartile range (IQR), whiskers extend to the last data point within 1.5 IQR beyond the box, and dots are outlier points beyond that range. Blue lines are mean values of all model data, used as common cutoffs.

Supplementary References

47. Robin, G. D. Q. Velocity of radio waves in ice by means of a bore-hole interferometric technique. *J. Glaciol.* **15**, 151–159 (1975).
48. Kovacs, A., Gow, A. J. & Morey, R. M. The in-situ dielectric constant of polar firn revisited. *Cold Reg. Sci. Technol.* **23**, 245–256 (1995).
49. Jol, H. M. *Ground Penetrating Radar Theory and Applications*. (Elsevier, 2008).
50. Kozlov, A. I., Ligthart, L. P. & Logvin, A. I. *Mathematical and Physical Modelling of Microwave Scattering and Polarimetric Remote Sensing: Monitoring the Earth's Environment Using Polarimetric Radar: Formulation and Potential Applications*. (Springer Netherlands, 2001).
51. Rutishauser, A. *et al.* Characterizing near-surface firn using the scattered signal component of the glacier surface return from airborne radio-echo sounding. *Geophys. Res. Lett.* **43**, 12,502–12,510 (2016).
52. Heilig, A., Eisen, O., MacFerrin, M., Tedesco, M. & Fettweis, X. Seasonal monitoring of melt and accumulation within the deep percolation zone of the Greenland Ice Sheet and comparison with simulations of regional climate modeling. *The Cryosphere* **12**, 1851–1866 (2018).